Magnetoresistive sensors for industrial positioning applications

Guilherme Brites
Instituto Superior Técnico
(Dated: October 16, 2021)

This project aims to analytically simulate the response of AMR sensors to external magnetic fields generated by regular patterns in magnetic tape. The external magnetic field is calculated from the magnetic tape characteristics and averaged over the sensor volume. The response of the sensor is calculated with the Stoner-Wohlfarth model, from which the angle the magnetization acquires with the easy axis, due to the external magnetic field, is extracted. Two different materials were used for the sensor, one magnetically soft and one hard, to evidence their differences. Several practical aspects such as distance between the magnetic media and sensor, sensor orientation and tilt were tested.

I. INTRODUCTION

A. Motivation

There is a very large competitive demand for devices that have reduced size and cost and that can operate in harsh conditions, while still providing accurate results. One of the most commonly used solutions is optical devices, which guarantee high resolution and accuracy, but require bigger and more expensive equipment to operate in dirty environments, for example. Magnetoresistive (MR) devices have a clear advantage over optical devices in this sense [1]. These MR devices can be used in encoding and can be produced with micrometric (and even nanometric) sizes. They are easily mass produced with low costs and are highly sensitive to weak magnetic fields. The operation of these sensors is also unaffected by the presence of water, oils, or dust, unlike the optical devices. Anisotropic magnetoresistive (AMR) sensors have a very simple structure, made from ferromagnetic materials, such as Permalloy ($Ni_{0.8}Fe_{0.2}$), resulting in low production costs. AMR sensors have a very low power consumption and offer sensitivity to magnetic fields down to the nT [2][3]. Paired with a magnetic tape these sensors can be used for positioning applications in any industry, providing a low cost, yet accurate and reliable solution, offering spatial resolution down to the μm [1].

B. State of the Art

The applications of magnetic and magnetoresistive sensors are very broad and they are present in many industries. For example, vehicle detection or measuring rotation speeds and angles, positions or lengths and even electrical currents. These measurements using magnetoresistive sensors, however, are generally indirect. The sensors themselves only give information about surrounding magnetic fields, which then needs to be processed to obtain the relevant parameters [4].

1. Magnetic sensors

These sensors have evolved greatly in the past decades due to the progress in micro and nanofabrication, since the devices are comprised of single or multi-layer thin film structures. The most simple ones, with a single magnetic layer are the Planar Hall Effect (PHE) sensors and the Anisotropic Magnetoresistive (AMR) sensors, but there are more elaborate devices with multi-layer structures of more complex and diverse materials, making use of Giant Magnetoresistance (GMR) and Tunneling Magnetoresistance (TMR) effects. Nonetheless, there is still room for improvement and optimization of the sensors to each specific application. Some of the largest AMR coefficients recorded are around 6%, in Ni_xFe_{1-x} alloys [5].

2. Magnetic encoders

Magnetic encoders are devices capable of converting magnetic measurements into measurements of position, angle, speed and distance; typically composed of two elements: a magnetic sensor and a magnetic scale [6]. Linear encoders can be used for positioning and can work in two different ways: they can be incremental or absolute [7]. Incremental linear positioning is the simplest form and these encoders can be found in industries such as agriculture, surveillance cameras, medicine, electric motors, robotics and green energy.

II. BACKGROUND

A. Anisotropic Magnetoresistance

The Anisotropic Magnetoresistance has its origins in magnetotransport, more specifically in spin-orbit coupling, resulting from the difference in the s-d electron scattering cross section when the current direction is varied with respect to the orientation of the magnetically aligned atoms [8]. The resistance of the material will vary, depending on the angle between the directions of electrical current and the magnetization. It is also known

that the direction of the magnetization depends on the direction and strength of an applied external field. The resistance is then correlated with that external magnetic field [9]:

$$R \equiv R(H_{ext}) \tag{1}$$

The magnitude of the magnetoresistive effect can be calculated using equation (2) [9]:

$$MR = \frac{R_{max} - R_{min}}{R_{min}} = \frac{\Delta R}{R_{min}} \tag{2}$$

A simple way to describe and understand the AMR effect is through the Stoner-Wohlfarth model. In figure 1, the change in the direction of the magnetization is shown, as well as all the relevant parameters for calculations of the AMR effect using this model.

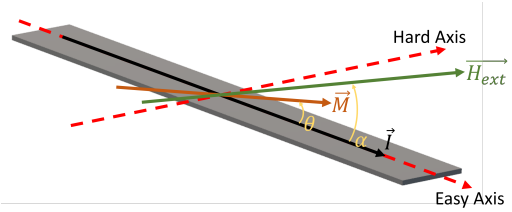

FIG. 1. Graphical representation of relevant parameters for AMR effect calculations, in a generic magnetic volume. Notice the angles θ between M and the easy axis, and α between H and the easy axis.

A thin film of ferromagnetic material has anisotropies that give rise to an easy and hard magnetic axis. The easy axis is the direction the magnetization will favour when there is no external magnetic field and the hard axis is perpendicular to that axis. Usually, in thin films, and such is the case in AMR sensors, these axes are in the plane of the film, due to a strong shape anisotropy. The magnetization will favour the easy direction and the hard direction can be considered the sensitive direction, since applying a magnetic field parallel to the easy axis will yield no change in the device, because the magnetization will not change orientation. The resistance of the device can be defined as a function of the angle θ between I and M as such:

$$R(\theta) = R_{min} + \Delta R \cos^2\theta \tag{3}$$

A solution can be derived for θ by minimizing the total magnetic energy of the layer:

$$E_T(\theta) = K_u sin^2\theta - \mu_0 M_s H_{\parallel} cos\theta - \mu_0 M_s H_{\perp} sin\theta \tag{4}$$

Where K_u is the uniaxial anisotropy constant of the thin film, with which the anisotropy field can be written as $H_k = \frac{2K_u}{\mu_0 M_s}$ and $H_{\parallel} = H_{ext}\cos\alpha$, $H_{\parallel} = H_{ext}\sin\alpha$. If the field is strong enough to saturate the device, the magnetization will acquire the direction of the magnetic field. In such case, $\theta = \alpha$, making possible then to measure the direction of the magnetic field, in the plane of the sensor. There are some disadvantages to these sensors, for example, their transfer curve is not linear

B. Magnetic scale

A magnetic scale is composed of magnetized pieces of a hard ferromagnetic material with identical sizes. The magnetized pieces will create a magnetic field in their proximity, which can be calculated using a fairly simple two dimensional model, assuming uniformity in the cross-track direction [10]:

$$H_n = -\frac{\sigma\Delta\theta}{2\pi} \tag{5}$$

$$H_t = -\frac{\sigma ln(r_1/r_2)}{2\pi} \tag{6}$$

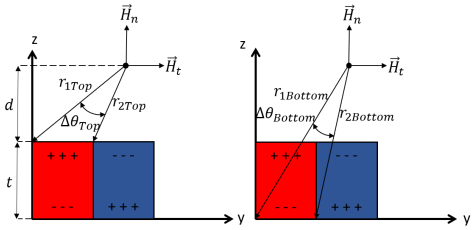

FIG. 2. Geometry for the calculation of the magnetic field generated by a magnetic scale, using a two dimensional model.

To complete the calculation, the two surfaces contributing to the field of each bit had to be taken into account, the *top* and *bottom* surfaces, and for the whole magnetic scale the contributions of each bit needs to be summed, resulting in equations (7) and (8), considering the scale has N bits.

$$H_n \equiv H_z(y,z) = \sum_{i=0}^{N-1} -\frac{\sigma^i \Delta\theta^i_{top}}{2\pi} + \frac{\sigma^i \Delta\theta^i_{bottom}}{2\pi} \tag{7}$$

$$H_t \equiv H_y(y,z) = \sum_{i=0}^{N-1} -\frac{\sigma^i ln(\frac{r^i_{2top}}{r^i_{1top}})}{2\pi} + \frac{\sigma^i ln(\frac{r^i_{2bottom}}{r^i_{1bottom}})}{2\pi} \tag{8}$$

Where $\sigma^i = \pm\sigma$ is the magnetic remanence of the bit, according to the direction of the magnetization. If the magnetization is along z, $\sigma^i = +\sigma$, if it is along $-z$, $\sigma^i = -\sigma$.
The two components $H_z(y,z)$ and $H_y(y,z)$ are in quadrature, which means the magnetic field is effectively rotating periodically, 360°. Figure 3 shows the vectorial plot of the magnetic field, over 4 bits of the scale, where the arrows indicate the direction of the magnetic field along y and z.

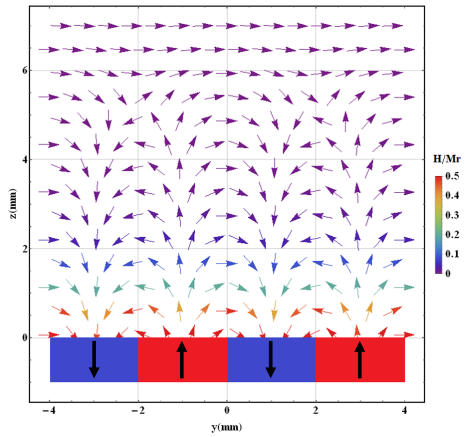

FIG. 3. Vectorial plot of the magnetic field generated by a magnetic scale. The intensity of the field is given as H/M_r (unitless). In this example the bit width is given as $w = 2mm$ and the thickness of the scale $t = 1mm$.

The magnetic field rotates 180° between each bit, and 360° between consecutive bits with the same magnetization. This is the key property that is exploited in order to create the incremental linear encoder, since the direction of the field changes linearly along the chosen flying direction.

C. AMR sensors for positioning

1. *Materials*

For AMR sensors, the materials used are typically *soft* magnetic materials. Under this denomination fall materials with low coercivity, high susceptibility and low magnetic remanence. In such materials, the processes through which the magnetization changes (domain wall motion and domain magnetization rotation) occur when applying external magnetic fields of low intensity, meaning very low fields are required to saturate the material[11]. Low coercivity will be very important for positioning applications. One example of such a material is permalloy (Py), an alloy of nickel and iron, $Ni_{0.8}Fe_{0.2}$, which has an anisotropy constant of $K_1 \approx -1kJ.m^{-3}$, a typical value for soft magnetic materials.

2. *Geometry*

Geometry is a key factor in AMR sensors. In order to exploit shape anisotropy, the sensors are fabricated according to some rules. The easy axis is defined mainly, through shape anisotropy: it will lie along the longest direction of the sensor. Therefore, the desired shape is a long and thin strip of material. However, one single strip of material does not provide enough sensing volume and has very low resistance, making it unsuitable for functioning as a sensor. To remedy that, a meander of strips is used, connected at alternate ends, as exemplified in figure 4, essentially creating a longer strip in a compact area [12] [13] .

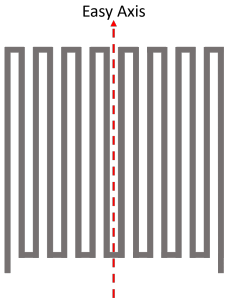

FIG. 4. Example of meander structure of AMR sensors.

A strip of the meander of AMR sensors follows the rule $a > b \gg c$, where for these dimensions the typical orders of magnitude are μm for a and b, and nm for c, corresponding to length, width and thickness.

3. *Configuration*

In positioning applications AMR sensors are connected in full-bridges, which are composed of four varying elements, in this case the AMR sensors, and provide a higher output and a better thermal compensation [12] [14] [15]. For positioning applications, two of these full bridges are used in each device, both biased by the same terminals. The electric schematic is represented in figure 5, and the outputs can be calculated using equation **??**, replacing the indexes for the correct resistances.

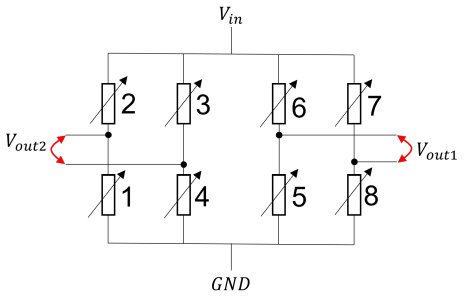

FIG. 5. Two full bridges with four varying components each, with a shared bias. Each component is an AMR sensor.

In each bridge, opposing sensors should be paired, being on the same state at any given instance.

D. Incremental Linear Encoders

The incremental linear encoder provides information on displacements from a reference, but is unable to provide an absolute position. The AMR sensors are used to sense the magnetic field generated by the scale and measure its direction, allowing an indirect measurement of a displacement. For this to be possible, the device needs to placed parallel to the $y0z$ plane, as indicated in figure 6:

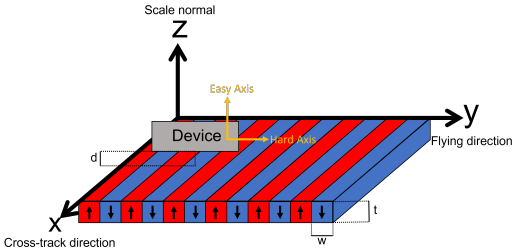

FIG. 6. Device and sensor placement over a magnetic scale, parallel to the $y0z$ plane. This placement allows the AMR sensors to measure the direction of the field. The device is placed at a distance d from the magnetic scale.

The transfer curve of the AMR sensor is not linear, and so will not be the output of eacg full bridge. The output is sinusoidal, which is not ideal for a linear positioning application. To achieve a linear output, two full bridges are used, which produce two sinusoidal outputs in quadrature due to the periodic properties of the magnetic scale. Figure 7 shows a compact arrangement of sensors that produce outputs in quadrature.

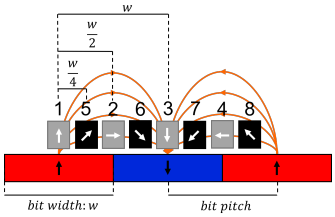

FIG. 7. Compact arrangement of AMR sensors in a linear positioning device, with two full bridges. Arrows in black represent the magnetization of the bits of the magnetic scale, arrows in white represent the magnetization of the AMR sensors. Sensors are numbered according to the numbering in figure 5.

.

Similarly to the magnetic field, two periodic signals in quadrature are generated, which means that taking their arc-tangent gives a linear signal. With a few more terms, as described in equation 9, it is then possible to calculate a linear displacement, based on the output of the two full bridges [16]:

$$X = \frac{w}{2\pi} \arctan\left(\frac{Bridge2}{Bridge1}\right) + \frac{w}{2}, \qquad (9)$$

where w is the scale period, or bit width, $Bridge1$ and $Bridge2$ are the outputs of the full bridges with sensors $S5$ to $S8$ and $S1$ to $S4$, respectively. This equation gives a relative position along one bit, from 0 to w.

III. IMPLEMENTATION

Sensors were fabricated at INESC-MN using two different buffer materials, Ta and NiFeCr, with varying thicknesses, in order to study its effect on the sensors' performance. The core of the sensor is a thin Permalloy film. Annealing was also introduced in the fabrication process to study its effect on the structural and magnetic properties of each stack. Figure 8 shows a schematic cross section of the finalized fabrication process.

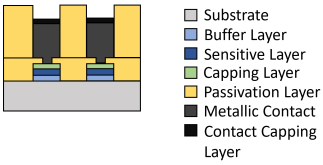

FIG. 8. Schematic cross section of the fabricated sensors.

A. Fabricated Samples

1. *Unpatterned Samples*

Four unpatterned samples were produced to study the effects of annealing time on the crystallographic structure of the material, mainly grain size and inter-planar distance. Table I summarizes the composition of these test samples. The samples are identified by their buffer layer description.

TABLE I. Composition different unpatterned test samples. Thickness between brackets given in Å.

Sample	Substrate	Buffer	Sensor	Capping
Ta(50)	Glass	Ta (50)	NiFe (400)	Ta (50)
NiFeCr(50)		NiFeCr (50)	NiFe (400)	
NiFeCr(100)		NiFeCr (100)	NiFe (400)	NiFeCr(50)
NiFeCr(150)		NiFeCr (150)	NiFe (300)	

2. *Patterned Samples*

Six samples were produced in total, on 1×1 inch samples, using the same fabrication process between them. Two were produced with the purpose of testing and comparing two different buffer materials: Ta and NiFeCr, with the same thickness. The other four samples have varying buffer thicknesses of NiFeCr. Table II summarizes the samples' compositions. The samples are iden-

tified by their buffer layer description. The first four samples are identical to the unpatterned samples made.

TABLE II. Composition different patterned test samples. Thickness between brackets given in Å.

Sample	Substrate	Buffer	Sensor	Capping
Ta(50)	$Si + SiO_2$	Ta (50)	NiFe (400)	Ta (50)
NiFeCr(50)		NiFeCr (50)	NiFe (400)	
NiFeCr(100)		NiFeCr (100)	NiFe (400)	NiFeCr(50)
NiFeCr(150)		NiFeCr (150)	NiFe (300)	
Ta(30)+NiFeCr(300)	$Si + SiO_2$	Ta (30) + NiFeCr (300)	NiFe (400)	NiFeCr(50)
NiFeCr(300)		NiFeCr (300)	NiFe (400)	

The samples were submitted to annealing with the parameters shown in table III. All the samples cooled down in a magnetic field of $1T$, with their easy axis aligned with the field.

TABLE III. Composition different test samples. Thickness between brackets given in Å.

Sample	Temperature (°C)	Duration (mins)
Ta(50)	350	120
NiFeCr(50)		
NiFeCr(100)		
NiFeCr(150)		
Ta(30)+NiFeCr(300)		30
NiFeCr(300)		

IV. RESULTS

A. X-Ray diffraction

The x-ray diffraction measurements give insight on the crystalline structure of the NiFe layer with *fcc* structure. The measured peaks correspond to diffraction on the [111] plane. The objective was to determine the effect of annealing on the grain size and inter-planar distance. For that purpose, the samples were submitted to several annealings, all at the same temperature of $350°C$. A total of four annealings were made, two of one hour, one of three hours and another of five hours, totalling up to ten cumulative hours of annealing.

1. *Diffraction peaks*

In figure 9, the detected diffraction peaks are plotted.

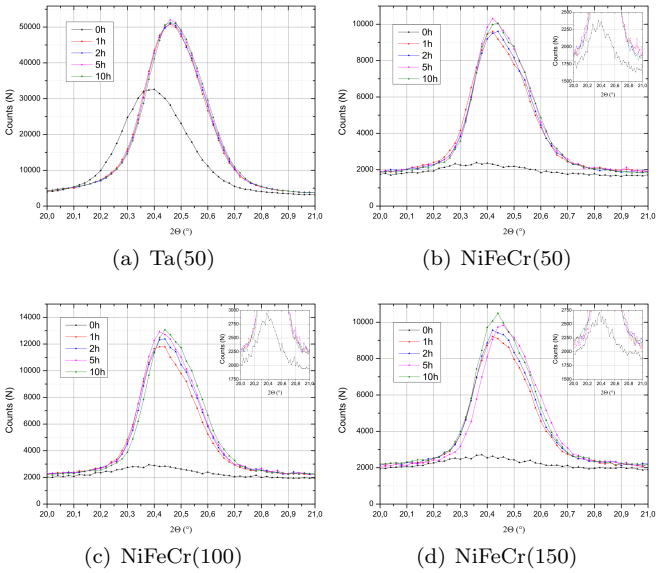

(a) Ta(50) (b) NiFeCr(50)

(c) NiFeCr(100) (d) NiFeCr(150)

FIG. 9. Evolution of X-ray diffraction peaks with cumulative annealing time.

On sample Ta(50), even before annealing the NiFe peak can be observed, meaning that the Ta buffer promotes a good crystalline growth on the NiFe film without additional aid from the annealing. The NiFeCr buffer samples show very similar results between them. There are no significant changes after the first hour of annealing and across the different NiFeCr samples the results are very similar, therefore independent of the buffer thickness.

2. *Grain size*

Grain size was calculated using equation the modified Scherrer equation (10), since the interest is only the grain size evolution:

$$\frac{\tau}{K} = \frac{\lambda}{FWHM\cos(\theta)} \tag{10}$$

Figure 10 shows the evolution of the grain size.

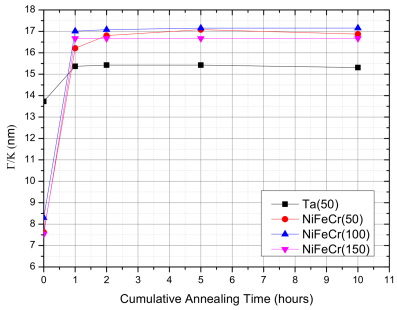

FIG. 10. Evolution of the grain size of all samples with cumulative annealing time.

Despite all samples displaying the same behaviour, the grain size increase is much larger in the NiFeCr samples.

3. *Inter-planar distance*

The variation of this quantity was very small, so the annealing had in fact little impact on the inter-planar distance, resulting in a variation of the order of the tenth of the *pm*, calculated with Bragg's equation: ´

$$d = \frac{\lambda}{2\sin(\theta)} \tag{11}$$

Figure 11 shows the evolution of the inter-planar distance.

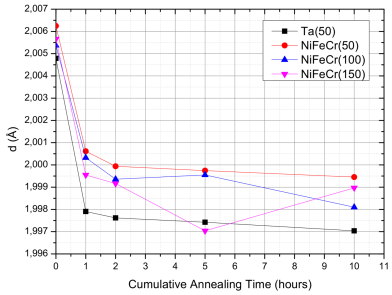

FIG. 11. Evolution of the inter-planar distance of all samples with cumulative annealing time.

B. Transfer Curves

The transfer curves of samples Ta(50), NiFeCr(50), NiFeCr(100) and NiFeCr(150) were taken before and after annealing. Due to the results from the x-ray diffraction analysis, the samples were annealed for two hours, which is enough time for the annealing to have its full effect, structurally, on the samples; the effects of annealing on the magnetic response remain unknown at this point. Samples Ta(30)+NiFeCr(300) and NiFeCr(300) were only measured after thirty minutes of annealing. The transfer curves are grouped and shown in figure 12:

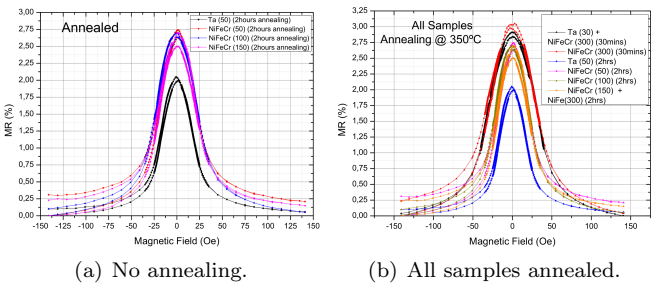

(a) No annealing. (b) All samples annealed.

FIG. 12. Transfer curves of samples without and with annealing.

Four parameters were extracted from the transfer curves: MR ratio, R_{min}, coercivity (H_C) and the FWHM of the curve. The results for all samples are shown in figure 13:

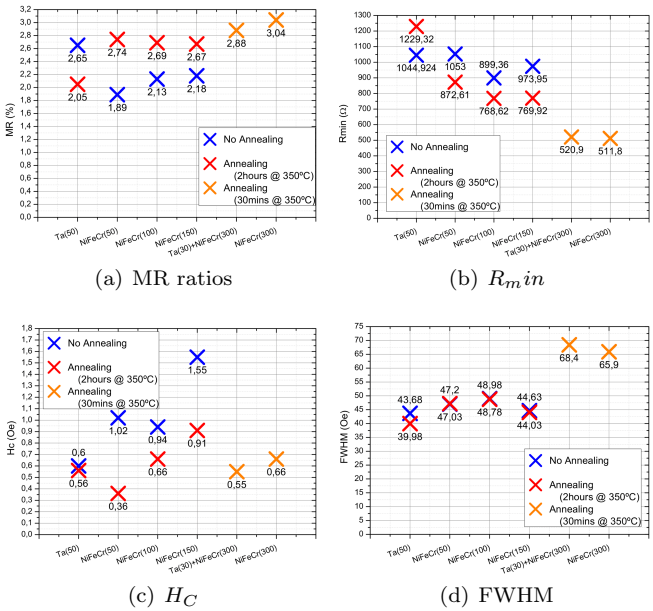

(a) MR ratios (b) R_min

(c) H_C (d) FWHM

FIG. 13. Trasnfer curve results before and after annealing.

The consequence of annealing (under the specified conditions) is completely opposite on the two different buffer materials, concerning MR ratios and resistance. The Ta(50) sample suffers a reduction of MR, down to 2%, where as the NiFeCr have their MR ratios increase up to around 2.75% to 3%. On the Ta(50) there is an increase in the resistance, while in the NiFeCr the resistance is lowered. In terms of coercivity, all samples improve with annealing, with the best result being obtained on the NiFeCr(50) sample, with $H_C = 0.36Oe$. The FWHM exhibits no significant change. For samples Ta(30)+NiFeCr(300) and NiFeCr(300) there is a significant increase in MR, with the latter surpassing a 3% MR ratio and the coercivity remains low. The main difference regarding the previous samples is the increase of the FWHM of the transfer curves. This parameter, relating to the saturation of the device, indicates that an higher field is required to saturate this sample.

C. Positioning

A scanning setup was adapted at INESC-MN to test the fabricated sensors, by designing and fitting a new acquisition board for measuring the full bridge outputs. Only three samples were chosen for testing: the Ta(50) was chosen, as it was the baseline stack for testing, along with sample NiFeCr(50) for a direct comparison, and lastly the sample Ta(30)+NiFeCr(300), because it had the highest FWHM. Two different designs had to be used

due to the reduced number of samples available, but very similar so still comparable. The scans were done over a $6mm$ span with a $10\mu m$ step and flying heights from $d = 0.2mm$ to $d = 2.0mm$ in a $0.2mm$ step. A sinusoidal wave was fit to each set of data to extract the relevant information. The polar plots with corrected offsets are shown in figures 14, 15 and 16.

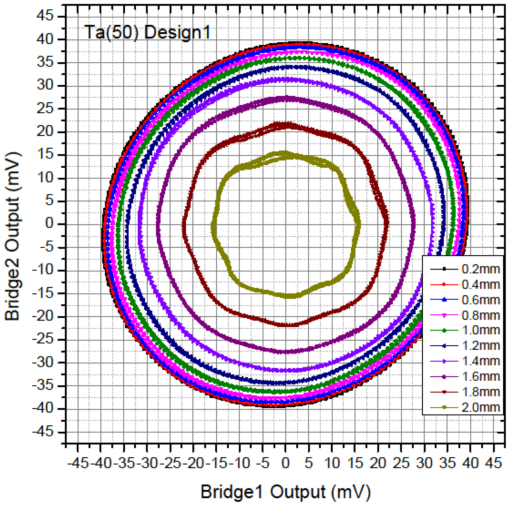

FIG. 14. Polar plots of sample Ta(50) at different flying heights.

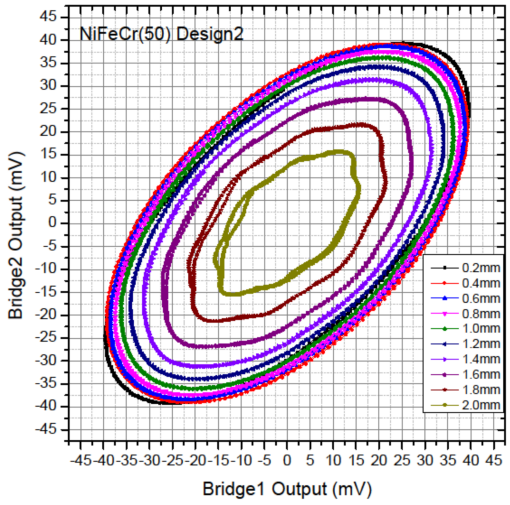

FIG. 15. Polar plots of sample NiFeCr(50) at different flying heights.

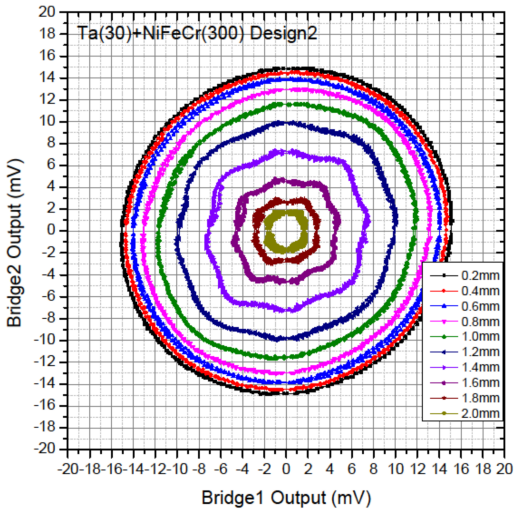

FIG. 16. Polar plots of sample Ta(30)+NiFeCr(300) at different flying heights.

Immediately, from all the plots it is possible to see that with increasing flying height, the amplitude of the bridge outputs decreases. Also noticeable is the fact that after a certain flying height, the polar plot loses its ideal circumference shape. This happens the earliest for sample Ta(30)+NiFeCr(300), at a flying height of $d = 1.2mm$.

1. *Bridge Offsets*

These offsets can result from the paired sensors having different resistance values, or different magnetic responses. The offsets are expected to be in the order of a few mV. The results regarding the offsets for the three tested samples are shown in figure **??**:

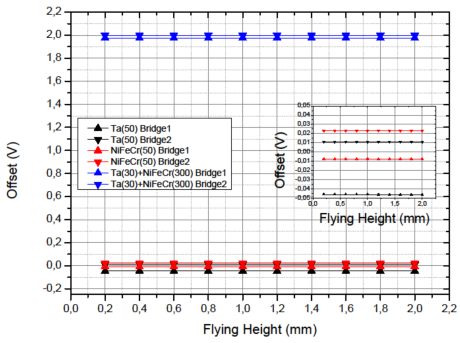

FIG. 17. Evolution of the offset of both bridges of each device with increasing flying height.

Sample Ta(30)+NiFeCr(300) exhibits a very abnormal behaviour, with a large offset of almost $2V$. The other two samples, Ta(50) and NiFeCr(50), have offsets within more reasonable values, although still high, $\approx -46mV$ and $\approx +11mV$ for sample Ta(50) and $\approx -7mV$ and

$\approx +22mV$ for sample Ta(50), for bridges 1 and 2 respectively. An important aspect of these measurements is that the offset of the bridges is unaffected by the increasing flying height.

2. Bridge Mismatches

Starting with the phase mismatch, a clear example occurred with sample NiFeCr(50). The phase difference between the two bridges, of the three samples, as a function of the flying height is shown in a plot in figure 18:

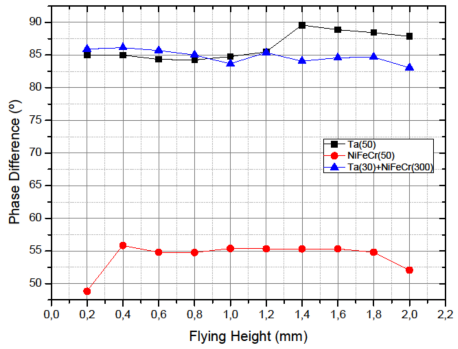

FIG. 18. Evolution of the phase difference with increasing flying height for the three tested samples.

Samples Ta(50) and Ta(30)+NiFeCr(300) show the values closest to the expected 90° phase difference. There is still phase mismatch however, as the phase difference is $\approx 85°$ for both. Sample NiFeCr(50) exhibits the largest phase mismatch, with a phase difference of $\approx 55°$. The phase difference remains similar throughout the different scans, so it is also unrelated to the flying height, and is again intrinsic to the sensor. This quantity should also be independent from the stack.
Now concerning amplitude mismatch the absolute values of the amplitude difference are plotted in figure 19:

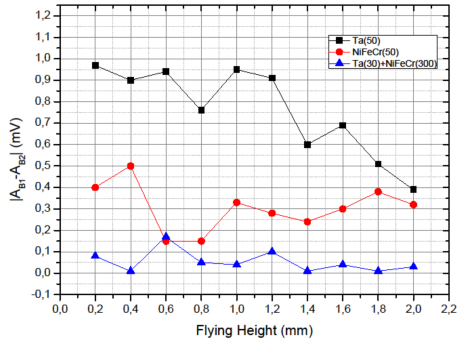

FIG. 19. Amplitude difference between bridges of the same device, as function of the flying height.

The device from sample Ta(50) shows the largest amplitude mismatch out of the three, with $\approx 1mV$ closest to the magnetic scale.

3. Positioning Error

After correcting the output of the bridges by subtracting the offset, the data was used to calculate the position of the sensor, relative to each bit, using equation 9. The performance was evaluated by comparing the increments in position, with the step used, by subtracting the $10\mu m$ step to the increment value obtained. The results for samples Ta(50) and NiFeCr(50) are shown in figure 20, for the first three flying heights, $d = 0.2mm$, $d = 0.4mm$ and $d = 0.6mm$. These two samples were chosen to be examined under the positioning error parameter because they exhibited an amplitude and phase mismatch. It is possible to examine the impact of these mismatches in the accuracy.

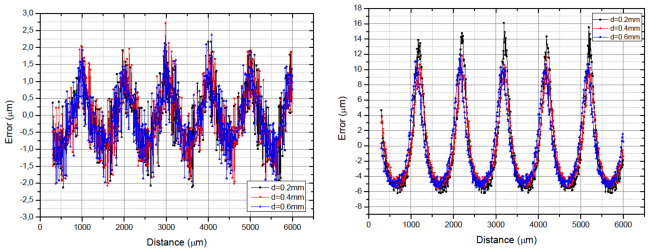

(a) Positioning error using devices from sample Ta50) at the first three flying heights.

(b) Positioning error using devices from sample NiFeCr(50) at the first three flying heights.

FIG. 20. Positioning error using devices from sample Ta(50) at the first three flying heights, $d = 0.2mm$, $d = 0.4mm$, $d = 0.6mm$.

Starting with the error value, sample the device from sample Ta(50) was the most accurate, with a maximum error of $\approx 2\mu m$, while sample NiFeCr(50) has a maximum error of $-15\mu m$. Another difference is that the positive and negative error are symmetric for sample Ta(50), $\approx \pm 2\mu m$, while for sample NiFeCr(50) this is not the case. The positive error has a maximum of $\approx +15\mu m$ and the negative error a maximum of $\approx -5\mu m$.
With the error values plotted, it is also clear that they have a semblance of periodicity. To evaluate this, a sinusoidal wave was again fitted to the data, to extract the period. This was done for the first three flying heights already mentioned, and the results were averaged and are presented in table IV:

TABLE IV. Average values of period, phase and phase difference of the positioning error, for the devices from samples Ta(50) and NiFeCr(50).

	Ta(50)	NiFeCr(50)	Difference
Period	502.58 ±1.75 (μm)	503.30 ±0.85 (μm)	
Phase	-45.18 ± 2.38 (°)	-16.50 ± 1.11(°)	28.68 ± 3.49 (°)

Regarding the period first, the error has a period of approximately half the signal period, so the maximum positive and negative errors occur periodically, twice per period of the bridge outputs. In other words, on one revolution around the polar plot, there will be two general areas, for positive and negative errors each, where the errors are maximized. Figure 21 shows the polar plots of samples Ta(50) and NiFeCr(50), at $d = 0.2mm$, with the points where the error is close to the maximum positive error (within 10% to 20% of the maximum value) marked in red, and where it is close to the maximum negative error marked in blue:

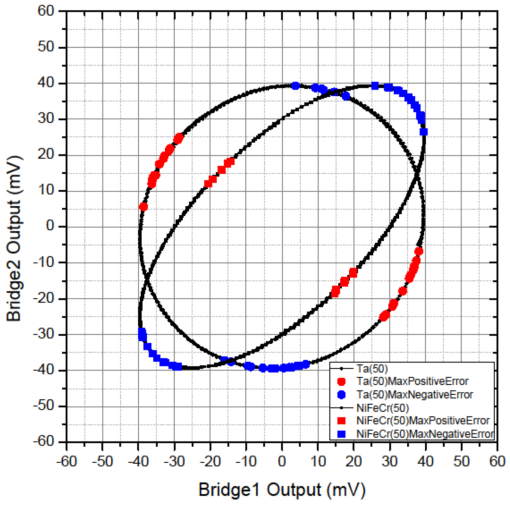

FIG. 21. Polar plot of measurements with the devices from samples Ta(50) and NiFeCr(50) with maximum positive and negative error zones highlighted.

The amplitude and phase mismatch are clear sources of error, as evidenced by these results. The elongation of the polar plot, from the perfect circumference to an ellipse, leads to an increased error in positioning. Also, it is possible to relate the sign of the error with the shape of the ellipse: points near the major axis have a default error and points near the minor axis have an excess error. In the case of the device from sample NiFeCr(50) this is very pronounced, since the phase shift is very large. In the device from sample Ta(50) there is a slight amplitude mismatch, higher amplitude on *Bridge*2, and the phase difference of the two bridges is not exactly 90°, so the circumference is slightly elongated in a direction near the y axis.

4. *Performance vs Flying Height*

By normalizing the amplitudes, it is possible to compare their evolution as function of flying height, directly across the three samples. The results are plotted in figure 22:

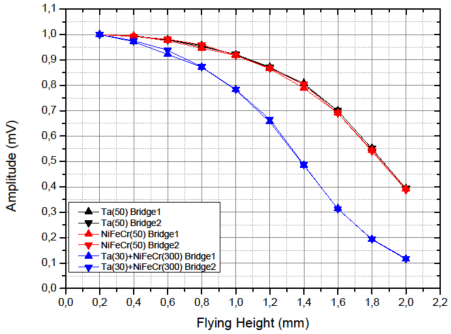

FIG. 22. Evolution of the normalized amplitude with increasing flying height.

The amplitude of the bridges from the device of sample Ta(30)+NiFeCr(300) drops much faster than that of the other samples. Since Ta(30)+NiFeCr(300) displayed the highest FWHM of the transfer curve, it requires a stronger magnetic field to saturate. The AMR sensors in this particular application are required to saturate, otherwise they do not function correctly and such is the case with the Ta(30)+NiFeCr(300): as the device is moved further from the scale, the amplitude drops significantly faster when compared with the other two samples. Regarding the other properties of the signals, period, phase and offset, no changes were verified when increasing the flying height. They are intrinsic to the geometry and bridge balance.
Plotting the maximum positive and negative positioning errors shows that for sample Ta(30)+NiFeCr(300) there is a clear dependence of the error with the flying height: the further away from the scale, the higher the error is. The devices from the other two samples have maximum errors approximately constant throughout the different flying heights, with a tendency to increase towards the largest flying heights, $d = 1.8mm$ and $2.0mm$, as can be seen on the plots in figure 23:

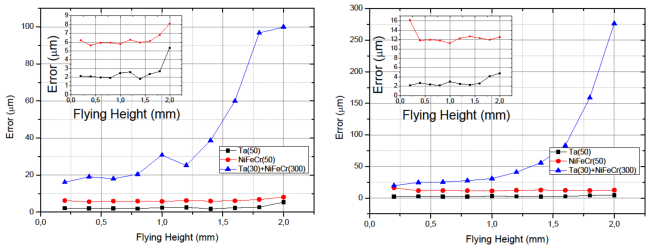

(a) Maximum positive positioning error.

(b) Maximum positive positioning error.

FIG. 23. Evolution of the maximum errors with increasing flying height.

The trend of increasing error with increasing flying height was observed in all cases, except for the maximum negative error in the device from sample NiFeCr(50), which actually had the largest error closest to the scale. More tests would be required to verify if this is an

anomaly, or it would be verified consistently. The plotted values being the maximum errors, they are sometimes larger than the actual step used, indicating that the flaws found are critical and must be addressed and minimized.

V. CONCLUSIONS

A. Achievements

It was possible to conclude that the magnetic annealing step is crucial when using NiFeCr as the buffer material. In these samples, a doubling of the grain size can be observed after one hour of annealing at 350°C. The process of annealing also showed improvements in the magnetic properties. The largest improvement was observed in the sample NiFeCr(50), from 1.89% to 2.74%. Overall, the MR ratio seems to increase with buffer thickness as well, as the highest MR ratio measured was 3.04% in sample NiFeCr(300). Resistance is in general lowered by annealing in NiFeCr samples, and as expected it also decreases with increasing total thickness. However, in Ta samples the annealing process has the opposite response: MR ratio decrease, while resistance increases.In all samples, annealing provided improvements in the coercivity. Whilst the saturation seems to not be influenced greatly by annealing, it seems to increase with increasing layer thickness.
The tests done with the scanner show that the setup, with the required adaptions to these sensors having been made, is suitable for detecting issues with the devices. It was possible to measure effectively the offsets of the bridges' outputs, by removing the common mode level, as well as amplitude and phase mismatches. The positioning error was also evaluated, and the sources of this error was successfully identified, as a relationship between mismatches and the positioning error was able to be drawn, from the tests on devices from samples Ta(50) and NiFeCr(50).

B. Future Work

There is no guarantee the behaviour observed in the tested samples would remain the same when annealing at different temperatures. It would be advantageous to find if there is an optimal annealing temperature, and not just duration at a single temperature. Also, a wider range of buffer thicknesses can be tested using NiFeCr, to obtain a more complete profile on the dependence of thickness of certain properties. With the testing setup now in place and properly working, what remains to do is further tests, with more devices from the same sample, and start to evaluate the effect of the stack on the several parameters that dictate the devices' performance for linear positioning. Further characterization can be made, regarding other important properties such as noise and thermal stability, for example, to provide a more complete picture on the quality of the sensors.

ACKNOWLEDGEMENTS

The author would like to thank Prof. Susana Cardoso de Freitas for the guidance during this work and INESC-MN for the resources made available.

[1] D. Collins, How do magnetic linear encoders differ from optical versions? (2018).
[2] J. M. D. Coey, *Magnetism and Magnetic Materials* (Cambridge University Press, 2010).
[3] M. Hott, P. A. Hoeher, and S. F. Reinecke, Magnetic communication using high-sensitivity magnetic field detectors, Sensors **19**, 3415 (2019).
[4] Q. Huang, A. H. Khawaja, Y. Chen, and J. Li, 2 state of the art magnetoresistance based magnetic field measurement technologies, in *Magnetic field measurement with applications to modern power grids* (John Wiley & Sons Ltd., 2020).
[5] T. McGuire and R. Potter, Anisotropic magnetoresistance in ferromagnetic 3d alloys, IEEE Transactions on Magnetics **11**, 1018 (1975).
[6] T. Costa, *Advanced Magnetoresistive Sensors for Industrial Applications*, Master's thesis, Instituto Superior Técnico (2017).
[7] Magnetic encoders balluff, https://www.balluff.com/.
[8] K. M. Krishnan, *Fundamentals and Applications of Magnetic Materials* (Oxford University Press, 2016).
[9] A. V. Silva, D. C. Leitao, J. Valadeiro, J. Amaral, P. P. Freitas, and S. Cardoso, Linearization strategies for high sensitivity magnetoresistive sensors, The European Physical Journal Applied Physics **72**, 10601 (2015).
[10] H. N. Bertram, *Theory of magnetic recording* (Cambridge University Press, 1994).
[11] R. C. OHandley, *Modern magnetic materials: principles and applications* (Wiley, 2000).
[12] L. Jogschies, D. Klaas, R. Kruppe, J. Rittinger, P. Taptimthong, A. Wienecke, L. Rissing, and M. C. Wurz, Recent developments of magnetoresistive sensors for industrial applications, Sensors **15**, 28665 (2015).
[13] L. Quynh, B. Tu, N. Thuy, D. Viet, N. Duc, A. Phung, and D. H. Giang, Meander anisotropic magnetoresistance bridge geomagnetic sensors, Journal of Science: Advanced Materials and Devices **4**, 327–332 (2019).
[14] R. Moghimi, Bridge-type sensor measurements are enhanced by autozeroed instrumentation amplifiers with digitally programmable gain and output offset, (2004).
[15] Wheatstone bridge circuit: Strain gauge, https://www.hbm.com/en/7163/wheatstone-bridge-circuit/ (2020).
[16] A. Voss, A. Meisenberg, and A. Bartos, Sacle based magnetoresistive sensor systems, TE Connectivity Sensor Solutions.